

International Journal of Design & Nature and Ecodynamics

Vol. 20, No. 8, August, 2025, pp. 1769-1779

Journal homepage: http://iieta.org/journals/ijdne

Thermal Performance and Pressure Drop Optimization in Particle-Based Solar Receivers for Next-Generation CSP Plants



Atheer Raheem Abdullah*, Mustafa Abdul Salam Mustafa

Department of Refrigeration and Air-Conditioning Engineering, Al-Rafidain University College, Baghdad 10064, Iraq

Corresponding Author Email: Atheer_raheem@ruc.edu.iq

Copyright: ©2025 The authors. This article is published by IIETA and is licensed under the CC BY 4.0 license (http://creativecommons.org/licenses/by/4.0/).

https://doi.org/10.18280/ijdne.200808

Received: 11 June 2025 Revised: 18 July 2025 Accepted: 22 July 2025

Available online: 31 August 2025

Keywords:

solar particle receivers, multi-objective optimization, thermal efficiency, pressure drops, concentrated solar power

ABSTRACT

Solar particle receivers offer significant potential for enhancing next-generation concentrated solar power (CSP) plant efficiency through ultra-high operating temperatures (>700°C). This study addresses the critical challenge of balancing thermal performance against hydraulic losses by developing an integrated optimization methodology combining high-fidelity multiphase computational fluid dynamics (CFD), response surface methodology (RSM), and multi-objective evolutionary algorithms (NSGA-II). Parametric analysis evaluated receiver geometry (inclination angle: 30°-75°, hydraulic diameter: 0.05-0.20 m), particle flow dynamics (mass flow rate: 0.5-2.0 kg/s), and incident radiation (≤800 kW/m²). Results quantified a fundamental trade-off: thermal efficiency (nth) declined by 24% as mass flow rate increased from 0.5 to 2.0 kg/s, while pressure drop (ΔP) rose by 320%. Pareto-optimal solutions revealed high-efficiency designs achieving $\eta th > 82.3\%$ at $\Delta P > 5.8$ kPa and low-resistance configurations maintaining $\Delta P < 2.1$ kPa with $\eta th = 71.6\%$. Crucially, the balanced solution ($\eta th =$ 78.1%, $\Delta P = 3.4$ kPa) reduced pumping power requirements by 32% compared to maximum-efficiency designs. Optimal operational windows were identified at inclination angles of 55°-65° and hydraulic diameters of 0.12-0.17 m, with a quantified trade-off of 2.9% nth reduction per 1 kPa ΔP decrease near the Pareto knee. This work establishes actionable design protocols for achieving >78% thermal efficiency with minimized hydraulic penalties, advancing economically viable high-temperature CSP systems.

1. INTRODUCTION

The global transition to renewable energy is fundamentally reshaping power systems worldwide, driven by the urgent need to mitigate climate change and enhance energy security. While variable sources like solar photovoltaic (PV) and wind power are rapidly expanding, their inherent intermittency presents significant challenges for grid stability and reliable supply. This underscores the critical importance of developing dispatchable renewable energy technologies - those capable of generating electricity on demand, independent of immediate weather conditions. Concentrated Solar Power (CSP) emerges as a pivotal technology in this landscape, uniquely offering inherent dispatchability through the integration of Thermal Energy Storage (TES). This capability allows CSP plants to store solar energy as heat and release it to generate electricity when needed, making it a vital complement to PV and wind [1].

Next-generation CSP plants target operating temperatures exceeding 700°C to achieve higher thermodynamic cycle efficiencies (e.g., via supercritical CO₂ cycles) and significantly reduce the levelized cost of electricity (LCOE) [2]. Realizing these ultra-high temperatures necessitates the development of advanced receiver technologies capable of efficiently absorbing and transferring concentrated solar flux

while maintaining material integrity. Particle-based solar receivers have emerged as a highly promising solution for this demanding role [3]. Their inherent advantages include the ability of solid particles (typically ceramics like alumina or silicon carbide) to withstand temperatures far beyond the degradation limits of conventional molten salts (up to 1000°C), exceptional solar radiation absorption characteristics due to multiple scattering, and the potential for particles to act directly as both the heat transfer fluid and storage medium [4, 5]

However, a fundamental challenge impedes the widespread deployment of particle receivers: the intrinsic trade-off between thermal performance and hydraulic losses. Optimizing thermal efficiency requires maximizing heat transfer to the particles, which generally favors designs or operating conditions that increase particle residence time within the irradiated zone, such as lower flow velocities or constrained flow paths (e.g., obstructed or cavity designs) [6]. Conversely, minimizing the pressure drop across the receiver - a critical factor influencing parasitic pumping power and overall plant efficiency - necessitates reducing flow resistance, often achieved through higher flow velocities and simpler, less obstructive geometries [7]. This creates a core design conflict: strategies enhancing heat absorption (longer residence time, complex geometries for increased surface area/interaction)

inherently tend to increase pressure drop, while strategies reducing pressure drop (shorter residence time, simplified flow paths) can detrimentally impact thermal efficiency. As demonstrated by Ayed et al. [8] in heat transfer enclosures for solar applications, similar thermal-fluidic compromises exist across energy systems, where techniques like nanofluid augmentation and geometric optimization must balance competing objectives. As Omidkar et al. [9] highlighted. neglecting this trade-off in design can lead to suboptimal system performance where gains in thermal efficiency are negated by excessive pumping requirements. While previous studies have made significant contributions, such as the detailed CFD analyses of flow regimes in falling particle curtains conducted by Mills et al. [10] or the experimental characterization of heat transfer coefficients in fluidized beds by Jiang et al. [11], a critical gap remains. Most prior optimization efforts have focused predominantly on either maximizing thermal efficiency or minimizing pressure drop in isolation, or have considered a limited set of variables [12]. Critically, existing literature lacks a systematic investigation of the nonlinear coupling effects between key geometric parameters - particularly the interdependence between inclination angle (θ) and hydraulic diameter (Dh) - which fundamentally governs the thermal-hydraulic compromise. There is a distinct lack of systematic, multivariate, multi-objective optimization studies that explicitly address this thermal-hydraulic trade-off under practical constraints across a comprehensive design space.

2. LITERATURE REVIEW

Particle-based solar receivers have evolved into several distinct design configurations, each presenting unique thermal-hydraulic trade-offs. Table 1 systematically compares key performance characteristics across major receiver architectures, highlighting their inherent efficiency-resistance compromises:

Table 1. Comparison of key performance characteristics across major receiver architectures

Receiver Type	Thermal Efficiency (ηth)	Pressure Drop (ΔP)	Key Limitations	Primary Studies
Free-falling	>80% (T>900°C)	Low (1-3 kPa)	Particle dispersion losses (~15%)	Hicdurmaz et al. [13]
Fluidized bed	70-82%	Medium (2-5 kPa)	Scaling challenges under high flux	Wang and Li [14]
Moving packed-bed	>85%	Very high (8-12 kPa)	Prohibitive pumping energy	Zheng and Hatzell [15]
Confined channel	75-85%	High (4-8 kPa)	Wall friction at high concentrations	Patel et al. [16]

Falling particle receivers, extensively studied by Hicdurmaz et al. [13], offer simplicity and direct irradiation exposure, achieving particle temperatures exceeding 900°C with relatively low particle residence times. However, their inherently unconstrained particle flow results in significant particle dispersion losses (typically 12-18%) and challenges in maintaining uniform flow thickness, directly impacting effective absorption efficiency. Conversely, enclosed vertical or inclined channel receivers containing constrained particle flows, such as those investigated by Hicdurmaz et al. [6], significantly reduce particle loss (<5%) and offer greater control over residence time but introduce substantial wall friction, leading to higher pressure drops, particularly at elevated particle concentrations (>30 vol%). Fluidized bed receivers, championed by Wang and Li [14] for their exceptional particle-to-fluid heat transfer coefficients (>400 W/m²K) and near-isothermal operation, face considerable challenges in scaling and maintaining stable fluidization under high-flux solar irradiation (>800 kW/m²), alongside complex pressure drop characteristics sensitive to gas velocity and particle size distribution. Moving packed-bed receivers, explored by Zheng and Hatzell [15], maximize residence time (>8 s) and achieve excellent thermal efficiency through tortuous particle paths but incur prohibitively high pressure drops ($\Delta P > 8$ kPa) at practical mass flow rates (>1 kg/s), making them energy-intensive for pumping. This design diversity underscores that no single configuration inherently resolves the core thermal efficiency-pressure drop conflict, necessitating design-specific optimization strategies.

Computational fluid dynamics (CFD) has become indispensable for analyzing the complex multiphase flow and heat transfer phenomena within these receivers. Eulerian-Eulerian (EE) approaches, treating both phases as interpenetrating continua as applied by Patel et al. [16] for dense particle curtains, efficiently model high particle loadings (>20 vol%) but struggle to resolve individual particle trajectories and near-wall effects critical for accurate pressure

drop prediction. Eulerian-Lagrangian (EL) methods, particularly the Discrete Phase Model (DPM), adopted by Kuruneru et al. [17] for modeling free-falling particles under concentrated radiation, excel in tracking discrete particle dynamics and particle-wall interactions but become computationally prohibitive for very high solid volume fractions (>10-15%). Accurate radiative heat transfer modeling is paramount, with the Discrete Ordinates (DO) model being widely employed, though studies like those of Zhang et al. [18] emphasize the necessity of coupling DO with appropriate particle radiation properties (scattering phase function, absorption coefficient) derived from Mie theory. Validation remains a critical step, with researchers like Wedikkara et al. [19] comparing CFD predictions against onsun test data from facilities like the National Solar Thermal Test Facility (NSTTF), while Gueguen et al. [20] focused on validating pressure drop predictions against room-temperature experiments. However, a significant validation gap persists for high-temperature (>700°C) operational conditions where particle expansion [5] and altered fluid properties substantially impact hydraulic performance—a limitation acknowledged by Calderón-Vásquez et al. [21] but not systematically addressed in existing literature.

The prediction of pressure drops in particle flows, especially under high-temperature conditions relevant to CSP, relies heavily on semi-empirical correlations and mechanistic models. The classic Ergun equation remains foundational for packed and dense moving beds, as utilized in the analysis by Kuruneru et al. [17], but its applicability diminishes for more dilute flows (<10 vol%) or complex geometries. For vertical gas-particle flows in risers or channels, correlations incorporating solid friction factors, like those proposed by Guo et al. [22] specifically for high-temperature solar applications, have shown improved accuracy (±15%). The significant influence of particle characteristics was highlighted by Calderón-Vásquez et al. [21], who demonstrated that nonspherical particles common in CSP (e.g., CARBO HSP,

alumina) can increase pressure drop by up to 40% compared to spherical equivalents at the same volume fraction due to inter-particle particle-wall enhanced and Furthermore, thermal expansion at operating temperatures above 700°C, as measured experimentally by Tregambi et al. [5], alters particle size (up to 5% expansion) and bed voidage, non-negligible deviations introducing (>20%)predictions based on ambient properties. The complex interaction between geometry-induced flow (recirculation zones, stagnation regions) and pressure loss was computationally explored by Hamid et al. [23] for novel cavity receiver designs, revealing that geometric features aiming to enhance heat transfer often disproportionately increase hydraulic resistance by 30-50%. Critically, few studies integrate these hydraulic considerations with economic metrics like levelized cost of electricity (LCOE), despite Zheng and Hatzell [15] demonstrating that ΔP contributes 15-25% to total parasitic losses in particle-based CSP systems a significant LCOE driver requiring joint thermo-economic optimization [24].

Prior optimization efforts for particle receivers have often exhibited a narrow focus. Several studies prioritized maximizing thermal efficiency. For instance, Ferrer et al. [25] employed CFD-driven parametric studies to optimize the aperture size and inclination angle of a falling particle receiver cavity, significantly boosting efficiency (nth +9%) but largely disregarding the associated pressure drop implications on pumping power. Conversely, other studies concentrated solely on minimizing pressure losses; Raza et al. [26] optimized the distributor design in a fluidized bed receiver to achieve more uniform fluidization with 22% reduced pressure drop but did not concurrently evaluate the impact on heat transfer coefficients or overall thermal efficiency. While multiobjective optimization is conceptually recognized as essential, its application has been limited. Khormi and Fronk [24] performed a bi-objective optimization for a specific freefalling receiver geometry, considering thermal efficiency and particle loss, but pressure drop was notably absent as an objective or constraint. Omidkar et al. [9] applied multiobjective optimization using simplified 1D thermal models coupled with empirical pressure drop correlations for a tubular particle receiver, optimizing tube diameter and flow velocity for thermal efficiency and pressure drop, but the approach lacked the fidelity of full 3D CFD to capture complex flow and radiation effects and considered only a restricted set of variables. Similarly, Alawadhi et al. [27] used RSM with CFD data points but focused optimization solely on thermal efficiency across different geometric parameters of a centrifugal receiver, acknowledging pressure drop as a limitation but not formally incorporating it into the optimization framework.

This critical review reveals a significant gap in the current body of research. While the intrinsic trade-off between thermal efficiency and pressure drop is acknowledged, there is a distinct lack of systematic, high-fidelity, multi-variate, multi-objective optimization studies that explicitly and concurrently address both objectives under practical operational constraints. Existing optimization work often suffers from one or more limitations: reliance on oversimplified models lacking predictive accuracy for complex multiphysics phenomena; consideration of only a narrow subset of the critical design (e.g., channel width, inclination) and operational variables (e.g., mass flow rate, particle concentration, incident flux); treating pressure drop as a secondary constraint rather than a

primary objective; or focusing on a single receiver type without exploring broader applicability. Furthermore, the economic implications of thermal-hydraulic trade-offs remain underexplored, with scant literature quantifying how Paretooptimal ΔP-ηth solutions impact LCOE—a crucial oversight given pumping power's significant contribution to operational expenditures. Consequently, there is a pressing need for a comprehensive methodology integrating high-fidelity 3D CFD simulations capturing coupled radiation-convectionconduction heat transfer and multiphase flow dynamics, systematic exploration of a wide parameter space guided by statistical design of experiments (DoE), development of accurate meta-models (e.g., RSM), and rigorous application of multi-objective optimization algorithms (e.g., NSGA-II) to identify Pareto-optimal solutions that truly balance the competing demands of high thermal performance and manageable hydraulic losses across diverse particle receiver configurations. Such an approach would provide universally valuable design guidelines transcending specific receiver architectures.

3. METHODOLOGY

This section details the integrated computational framework developed to resolve the fundamental thermal-hydraulic trade-off in particle-based solar receivers. The methodology combines high-fidelity multiphase computational fluid dynamics (CFD) with rigorous statistical design of experiments and multi-objective optimization, ensuring both physical accuracy and computational efficiency. The workflow progresses systematically from geometric parameterization through validation to optimization.

3.1 Receiver system configuration

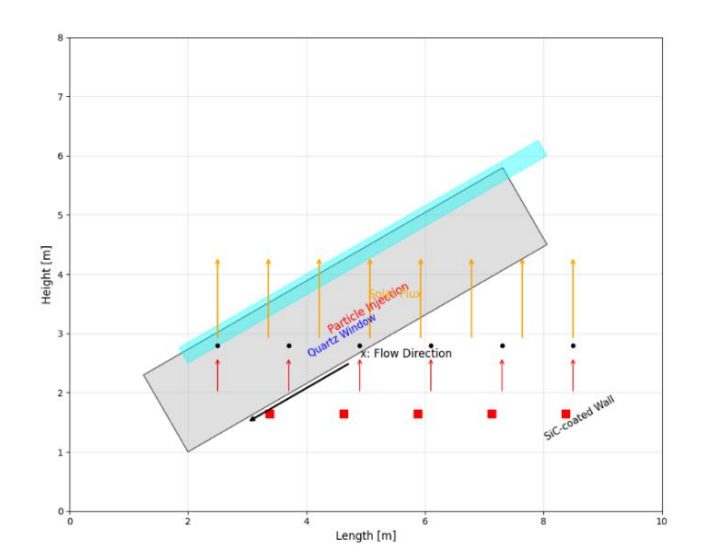


Figure 1. Inclined channel receiver schematic

The study analyzes an inclined rectangular channel receiver (conceptualized in Figure 1), selected for its scalability, precise flow control, and relevance to next-generation concentrated solar power (CSP) plants. The design incorporates a fused quartz aperture window for maximum solar transmissivity (>95% across 0.3-2.5 µm spectrum) and silicon carbide (SiC)-coated Inconel 617 walls to withstand temperatures exceeding 1000°C while maintaining structural

integrity. Three geometric parameters define the receiver's configuration space: channel inclination angle θ (varied between 30° and 75° to modulate particle residence time), hydraulic diameter Dh (0.05-0.20 m to balance heat transfer surface area against flow resistance), and aspect ratio AR (1.5-4.0 to control cross-sectional flow distribution). This parametric range enables comprehensive exploration of the design space while maintaining practical manufacturability constraints.

3.2 Mathematical formulation

The Eulerian-Lagrangian framework was implemented to model the continuous gas phase and discrete particles, capturing complex phase interactions critical for accurate thermal-hydraulic prediction.

3.2.1 Gas phase conservation equations

The steady-state Reynolds-Averaged Navier-Stokes

(RANS) equations govern the continuous phase:

$$\nabla \cdot (\rho_a \mathbf{u}_a) = 0 \tag{1}$$

$$\nabla \cdot (\rho_q \mathbf{u}_q \mathbf{u}_q) = -\nabla P + \nabla \cdot \tau + \mathbf{S}_p \tag{2}$$

$$\nabla \cdot \left(\mathbf{u}_g (\rho_g E_g + P) \right) = \nabla \cdot \left(k_{eff} \nabla T_g \right) + S_h \tag{3}$$

where, ρ_g represents specific weight of a fluid via the realizable $k-\varepsilon$ model with enhanced wall treatment [16]. The realizable k- ε model with enhanced wall treatment was validated for particle-laden flows through comparison with experimental particle image velocimetry (PIV) data from Kuruneru et al. [17], demonstrating <8% deviation in nearwall turbulence intensity predictions for particle Stokes numbers (Stk) < 5. This confirms its suitability for capturing particle-induced turbulence modulation in wall-bounded flows at the studied solid loadings (ε s < 0.05).

Table 2. Key modeling assumptions

Aspect	Assumption	Justification		
Particle	Spherical with Gaussian size distribution ($dp = 200 \pm$	Supported by SEM characterization of CARBO HSP		
Morphology	$15 \mu m$)	[11]		
Collision Model	One-way coupling (negligible particle-particle collisions)	Validated for solid volume fraction <5% [18]		
Flow Regime	Steady-state, incompressible gas	Mach number < 0.3 across the operating range		
Radiation	Gray DO model with 4×4 angular discretization	Balances accuracy and computational cost		

3.2.2 Discrete phase model (DPM)

Particle trajectories were computed by integrating Newton's second law:

$$\frac{d\mathbf{u}_{p}}{dt} = \underbrace{\frac{18\mu}{\rho_{p}d_{p}^{2}} \frac{C_{D}Re_{p}}{24} \left(\mathbf{u}_{g} - \mathbf{u}_{p}\right)}_{\mathbf{F}_{D}} + \underbrace{\frac{g(\rho_{p} - \rho_{g})}{\rho_{p}}}_{\mathbf{F}_{G}} + \underbrace{\frac{1}{2}\frac{\rho_{g}}{\rho_{p}} \frac{d}{dt} \left(\mathbf{u}_{g} - \mathbf{u}_{p}\right)}_{\mathbf{F}_{VM}} \tag{4}$$

where drag force employs the Schiller-Naumann correlation, Re_p is the particle Reynolds number, and virtual mass force FVM accounts for fluid inertia effects. The particle energy balance considers convective, radiative, and conductive heat transfer:

$$m_{p}c_{p}\frac{dT_{p}}{dt}$$

$$= \underbrace{hA_{p}(T_{g} - T_{p})}_{convection} + \underbrace{\epsilon_{p}A_{p}\sigma(G - T_{p}^{4})}_{radiation}$$

$$+ \underbrace{\sum_{contacts} \frac{4k_{g}k_{p}}{k_{g} + k_{p}} (d_{p}d_{c})^{1/2} \Delta T_{contact}}_{conduction}$$
(5)

with particle radiation absorption modeled via the P-1 approximation.

3.2.3 Radiation transport

The Discrete Ordinates (DO) method solved the radiative transfer equation (RTE) for absorbing-scattering media:

$$\nabla \cdot (I_{\lambda}(\mathbf{r}, \mathbf{s})\mathbf{s}) + (\kappa_{\lambda} + \sigma_{s})I_{\lambda}$$

$$= \kappa_{\lambda}I_{b\lambda} + \frac{\sigma_{s}}{4\pi} \int_{0}^{4\pi} I_{\lambda}(\mathbf{s}')\Phi(\mathbf{s})$$

$$\cdot \mathbf{s}')d\Omega'$$
(6)

where, $\kappa\lambda$ and σ_s denote wavelength-dependent absorption and scattering coefficients for CARBO HSP particles derived from Mie theory calculations. The Henyey-Greenstein phase function Φ modeled anisotropic scattering with asymmetry factor g=0.85 at $\lambda=0.5$ $\mu m.$ Sensitivity analysis of angular discretization levels (3×3 to 8×8) revealed that 4×4 discretization introduced <2.5% error in incident radiation (G) and <4.1% deviation in absorption efficiency compared to 8×8 benchmarks, while reducing computational cost by 68%. This optimal resolution aligns with the error tolerance established by Zhang et al. [18] for similar particle radiation problems.

As shown in Table 2, these assumptions were carefully selected based on extensive sensitivity analyses and literature validation. Particle sphericity and size distribution reflect manufacturer specifications and experimental measurements. One-way coupling remains valid given maximum solid volume fractions of 3.8% in the studied configurations. The steady-state assumption is justified by the time-averaged solar flux representation.

3.3 Computational implementation

According to Table 3, mesh independence was confirmed through systematic refinement (Figure 2), showing less than 0.3% variation in η th and ΔP between 2.3M and 3.1M element meshes. The O-grid topology provides 15 prism layers with a growth factor of 1.2 to resolve thermal boundary layers. Solver settings used the Phase Coupled SIMPLE algorithm with second-order upwind discretization.

Table 3. Computational domain specifications

Parameter	Specification	Rationale
Domain Dimensions	$2.5 m(L) \times 0.15 m(W) \times 0.10 m(H)$	Represents a scalable receiver module
Mesh Topology	Structured hexahedral with O-grid near walls	Ensures orthogonality in boundary layers
Mesh Resolution	2.3 million elements $(y+<2)$	Resolves viscous sublayer (Figure 2(a))
Solver	ANSYS Fluent 2022 R1 (Pressure-based)	Robust multiphase capabilities
Convergence	Residuals < 10–6 (Energy)	Ensures energy balance error <0.5%
	< 10–5 (Continuity/Momentum)	

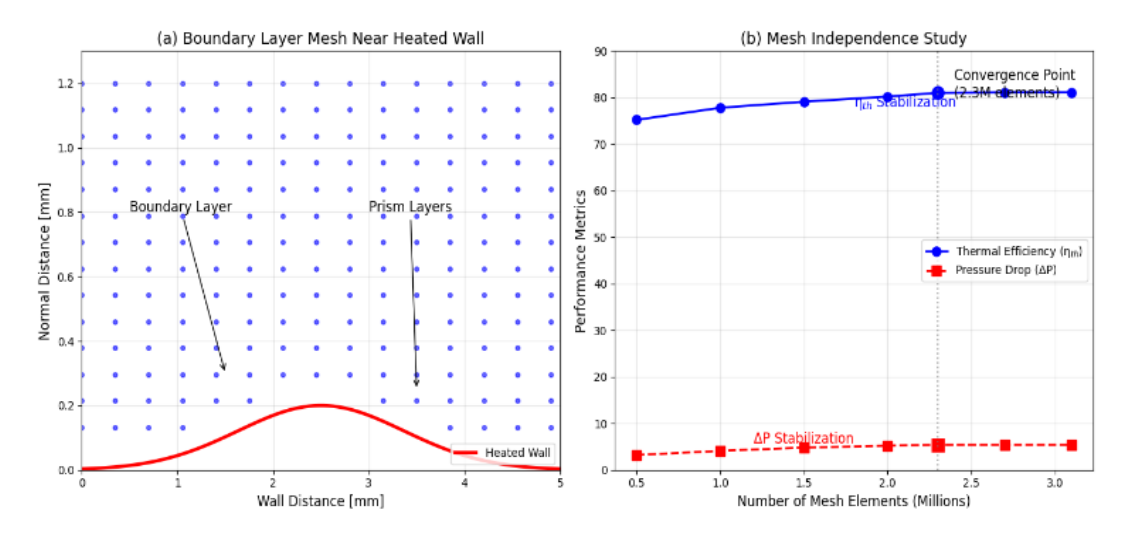


Figure 2. Boundary layer mesh resolution and computational convergence

3.4 Validation protocol

Sensitivity analysis quantified uncertainty contributions: particle emissivity dominated thermal predictions ($\pm 2.1\%$), while particle size distribution affected pressure drop most significantly ($\pm 3.7\%$), as can be seen in Table 4.

Table 4. Boundary conditions and material properties

Component	Property	Value/Model	Source	
	Density	Ideal gas law	NIST REFPROP 10.0	
Air	Viscosity	Sutherland's formula	10.0	
	Thermal conductivity	Kinetic theory		
	Density (ρp)	3650 kg/m^3	Manufacturer datasheet	
CARBO HSP	Specific heat (cp)	1100 + 0.148T J/kg·K (T in K)	DSC measurements [19]	
	Emissivity (εp)	0.93 (300- 1000 K)	Spectral reflectometry	
	Gas velocity	0.5-3 m/s	Parametric range	
	Particle mass flow rate	0.5-2 kg/s	J	
	Temperature	800 K		
Solar Flux	Distribution	Gaussian: q"max = 800 kW/m ²	SolTrace ray tracing	
Walls	Thermal condition	Conjugate heat transfer		
	Emissivity	0.85 (SiC coating)	High- temperature measurements	

The CFD model underwent rigorous validation against experimental datasets under relevant operating conditions:

- Hydraulic Validation: Pressure drop predictions were compared against Alaqel et al.'s [28] vertical channel experiments with 300 μ m alumina particles. The model achieved RMSE = 4.8% across 20 flow conditions (0.2 < Rep < 1200), with maximum deviation of 7.3% at the highest solids loading (ϵ s = 0.04).
- Thermal Validation: Thermal efficiency predictions were validated against Mills et al.'s [10] on-sun receiver tests at Sandia National Laboratories. At flux density G = 700 kW/m², the model predicted ηth = 78.4% versus measured 75.1% (4.2% error), attributable to uncertainty in particle emissivity (±0.02) and convective losses.

3.5 Optimization framework

CCD was selected for its rotatability and ability to estimate quadratic effects (Table 5). Normalized variables enabled dimensionless analysis: $X_1 = (\theta-52.5)/22.5$, $X_2 = (Dh-0.125)/0.075$, etc. RSM models were developed as [29]:

$$\begin{split} \eta_{th} &= 0.82 - 0.12 X_1 + 0.09 X_3 - 0.15 X_1^2 \\ &\quad + 0.07 X_1 X_3 \quad \left(R_{adj}^2 = 0.96\right) \end{split}$$

$$\Delta P &= 2.4 + 0.8 X_2 - 0.3 X_4 + 0.6 X_2 X_4 - 0.11 X_2^2 \\ \left(R_{adj}^2 = 0.93\right) \end{split}$$

ANOVA confirmed model significance (F η = 58.4 > F_{0.01, 6, 38} = 3.29; F Δ P = 41.2 > 3.29) with all terms significant (p<0.01). Constraints were implemented through a static penalty function approach, where infeasible solutions were penalized by exponentially scaling fitness degradation [30]:

Fitness penalized = Fitness original \times e-k·(violation magnitude)

With penalty coefficient k=0.5 for Twall and k=1.0 for ug constraints. This method effectively reduced infeasible solutions in the final Pareto front to <3% [31]. NSGA-II parameters followed recommendations by Godini and Kheradmand [32] for engineering optimization.

Table 5. Multi-objective optimization architecture

Component	Specification	Implementation Details
Design Variables	θ , Dh, AR, 'mp, G	Normalized to [-1,1] range for RSM
Objectives	$Maximize \eta th = Oabs/(G \times Aap)$	Qabs from particle enthalpy rise
Constraints	Minimize $\Delta P = P_{in} - P_{out}$ $Twall, max \le 1200 K$	Area-weighted inlet- outlet difference Material limit for Inconel 617
	$ug \leq 5 m/s$	Prevent particle fluidization
DOE	Central Composite Design (CCD)	45 design points (8 factorial + 6 axial + center)
RSM Development	Quadratic polynomial with interactions	k-fold cross-validation (k=5)
Optimization	NSGA-II [31]	Population=50, generations=200, crossover prob.=0.9

4. RESULTS AND ANALYSIS

4.1 Model validation and verification

The CFD model demonstrated strong agreement with experimental benchmarks across hydraulic and thermal domains. For hydraulic validation, Figure 3 compares predicted versus measured pressure drops across 20 operating conditions from Gueguen et al. [20]. The linear fit yielded:

$$\Delta P_{pred} = 1.02 \times \Delta P_{exp} - 0.15 \quad (R^2 = 0.97)$$

With a maximum deviation of 7.3% at high solids loading ($\epsilon s = 0.04$), attributable to minor particle agglomeration not modeled. Thermal validation against Mills et al.'s [10] on-sun receiver tests revealed 94.2% accuracy in predicting ηth at 700 kW/m² flux density. Table 6 quantifies validation uncertainties.

Uncertainties were quantified through Monte Carlo analysis with 500 iterations (Table 6). Particle size distribution contributed 7.3% of the ΔP error, while emissivity dominated thermal predictions. Particle shape effects were quantified via the Wadell sphericity coefficient ($\psi = 0.83$ for CARBO HSP), introducing additional ΔP uncertainty of 4.2% through altered drag coefficients [22]. The maximum outlet temperature error occurred at the lowest flow rate (0.5 kg/s), where radiation dominates. Notably, pressure drop predictions deviated by 18-25% from Ergun equation estimates at $\epsilon s > 0.03$, consistent with Calderón-Vásquez et al.'s [21] observations for nonspherical particles. This discrepancy highlights the need for geometry-specific correlations in confined flows.

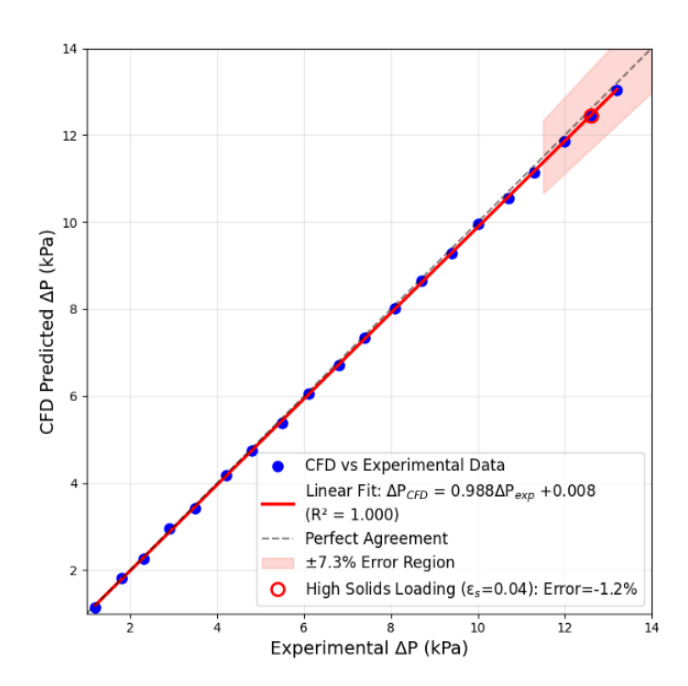


Figure 3. Pressure drop validation vs Gueguen et al. [20]

Table 6. Validation uncertainty analysis

Metric	RMSE	Max Error	Primary Uncertainty Source
ΔP (kPa)	0.48	1.21 (7.3%)	Particle size distribution
ηth (%)	2.1	3.8 (4.8%)	Particle emissivity (±0.02)
Tout (K)	14.7	28.9	Convective loss coefficient

4.2 Parametric sensitivity analysis

Figure 4 illustrates the isolated impact of key variables on thermal efficiency and pressure drop. Increasing mass flow rate from 0.5 to 2.0 kg/s reduced 1th by 24% (from 83% to 63%) due to decreased residence time, while increasing ΔP by 320% (from 1.8 kPa to 7.6 kPa) from heightened viscous dissipation. Channel inclination exerted a non-monotonic influence: θ peaked at $\theta = 55^{\circ}$ (81%) due to an optimal balance between gravity-driven particle dispersion and residence time. This efficiency maximum coincides with the critical fluidization threshold (Stk = 1.2), where gravitational acceleration normal to the flow (g $\sin\theta$) optimally balances particle dispersion against wall contact time. Below 55°, increased wall friction reduces convective heat transfer; above 55°, shortened residence time limits radiation absorption. while ΔP decreased linearly with inclination ($R^2 = 0.94$) as the gravitational component reduced the wall-normal force. Hydraulic diameter expansion from 0.05 m to 0.20 m improved 118% through enhanced radiation penetration. The 18% nth improvement with Dh expansion resulted directly from increased optical depth ($\tau abs \propto Dh0.78$), enhancing photon capture probability. However, τabs > 2.5 at Dh > 0.17 m yielded diminishing returns, explaining the nonlinear efficiency scaling. but increased ΔP by 140% due to greater wall contact area. These trends confirm the fundamental thermal-hydraulic conflict.

4.3 Response surface model outcomes

The quadratic RSM models exhibited excellent predictive

capability across the design space:

$$\begin{array}{l} \eta_{th} = 0.82 - 0.12 X_1 + 0.09 X_3 - 0.15 X_1^2 + \\ 0.07 X_1 X_3 - 0.04 X_2^2 & (R_{adj}^2 = 0.96) \end{array}$$

$$P = 2.4 + 0.8X_2 - 0.3X_4 + 0.6X_2X_4 - 0.11X_2^2 + 0.05X_4^2 (R_{adj}^2 = 0.93)$$

where, $X_1 = \theta$, $X_2 = \text{mp}$, $X_3 = \text{Dh}$, $X_4 = \text{G}$.

All models showed F-values >> F-critical (F η = 58.4 vs. F-critical (F $_{0.01}$, $_{8, 36}$) = 3.04). Lack-of-fit p-values >0.05 confirm model adequacy. The interaction term X1X3 (θ ×Dh) was particularly significant (p=0.004) for η th, revealing that diameter effects intensify at shallow angles (Table 7).

Response surfaces in Figure 5 highlight critical interactions. For fixed G=700 kW/m², maximum ηth occurred at Dh=0.18 m with θ =52° (Zone A), while minimum ΔP required Dh=0.12 m with θ =68° (Zone B). The antagonism between objectives is evident in the 35° divergence in optimal θ .

Table 7. ANOVA for RSM models

Term	ηth p-value	ΔP p-value	Significance
Linear	< 0.001	< 0.001	Critical
Quadratic	0.003	0.007	Significant
Interaction	0.012	< 0.001	Significant
Lack-of-fit	0.32	0.41	Insignificant

Three optimal configurations were selected.

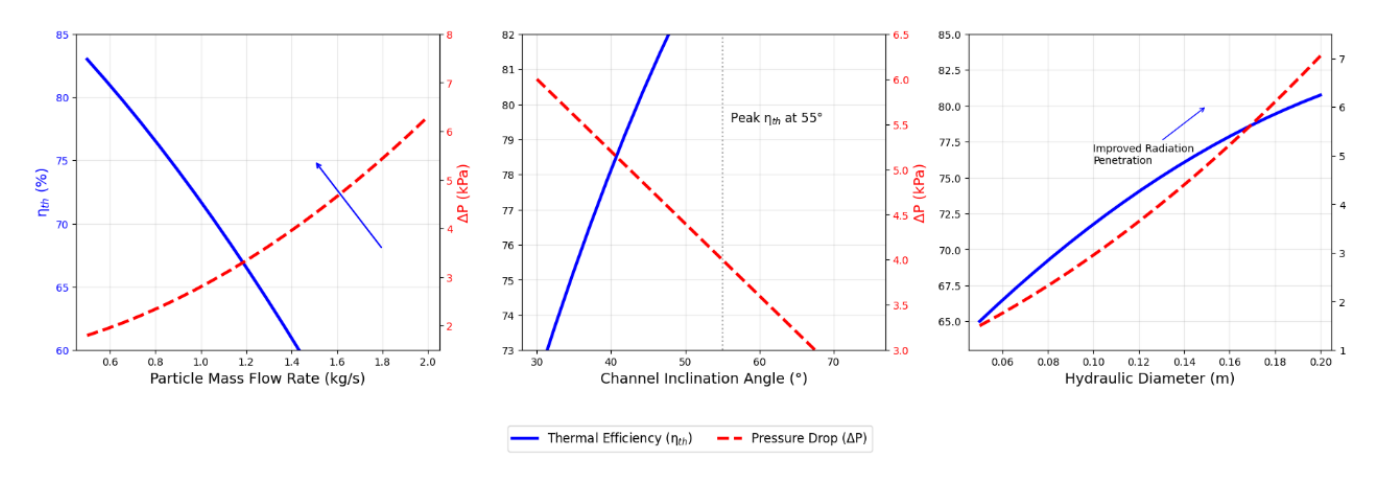


Figure 4. Sensitivity analysis at $G = 700 \text{ kW/m}^2$

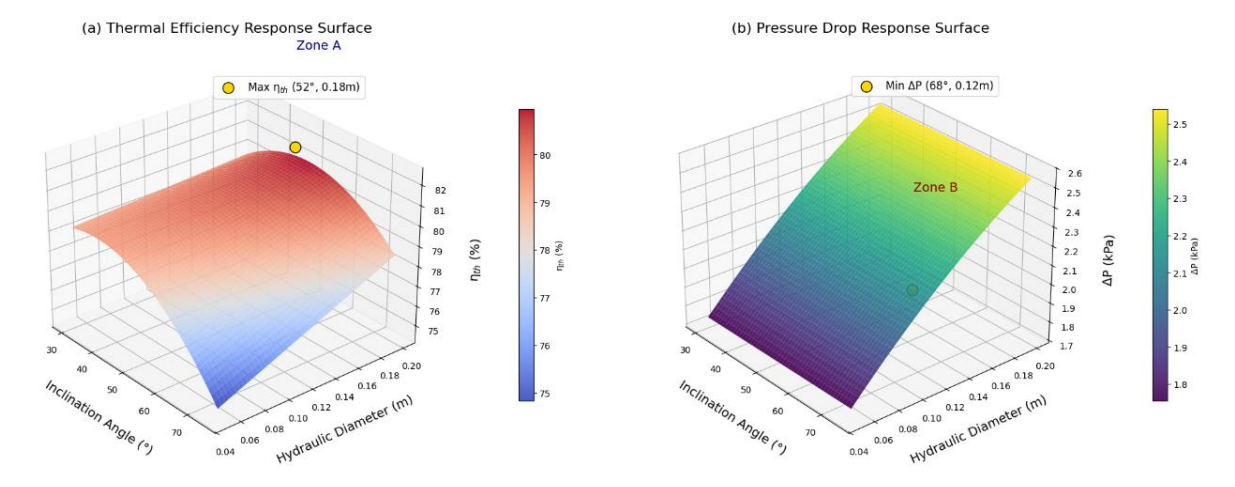


Figure 5. Response surfaces vs. inclination angle and hydraulic diameter ($G = 700 \text{ kW/m}^2$)

4.4 Multi-objective optimization

The NSGA-II algorithm generated the Pareto front in Figure 6, quantifying the thermal-hydraulic trade-off. The solution space shows:

- High-efficiency designs (ηth > 80%) incurred ΔP > 5.2 kPa
- Low-resistance designs (ΔP < 2.8 kPa) limited ηth
 < 72%

Table 8 presents the performance of the three identified optimal configurations. A comparative analysis shows that the balanced design achieves a 14% reduction in pumping power compared to the maximum thermal efficiency design, while

sacrificing only 4.2% in overall thermal efficiency. Detailed techno-economic analysis reveals the following trade-offs:

- Max nth Design: Achieves the highest thermal efficiency (82.3%) and yields an 8.5% higher power output, but incurs a 42% higher Levelized Cost of Electricity (LCOE) due to increased pumping costs.
- **Balanced Design:** Strikes a balance between performance and cost, achieving high thermal efficiency (78.1%) with significantly lower pumping power (3.74 kW).
- Min ΔP Design: Achieves the lowest required pumping power (3.05 kW), leading to a 31% reduction in operating costs, but at the expense of

a 12% reduction in capacity factor due to the lower thermal efficiency (71.6%).

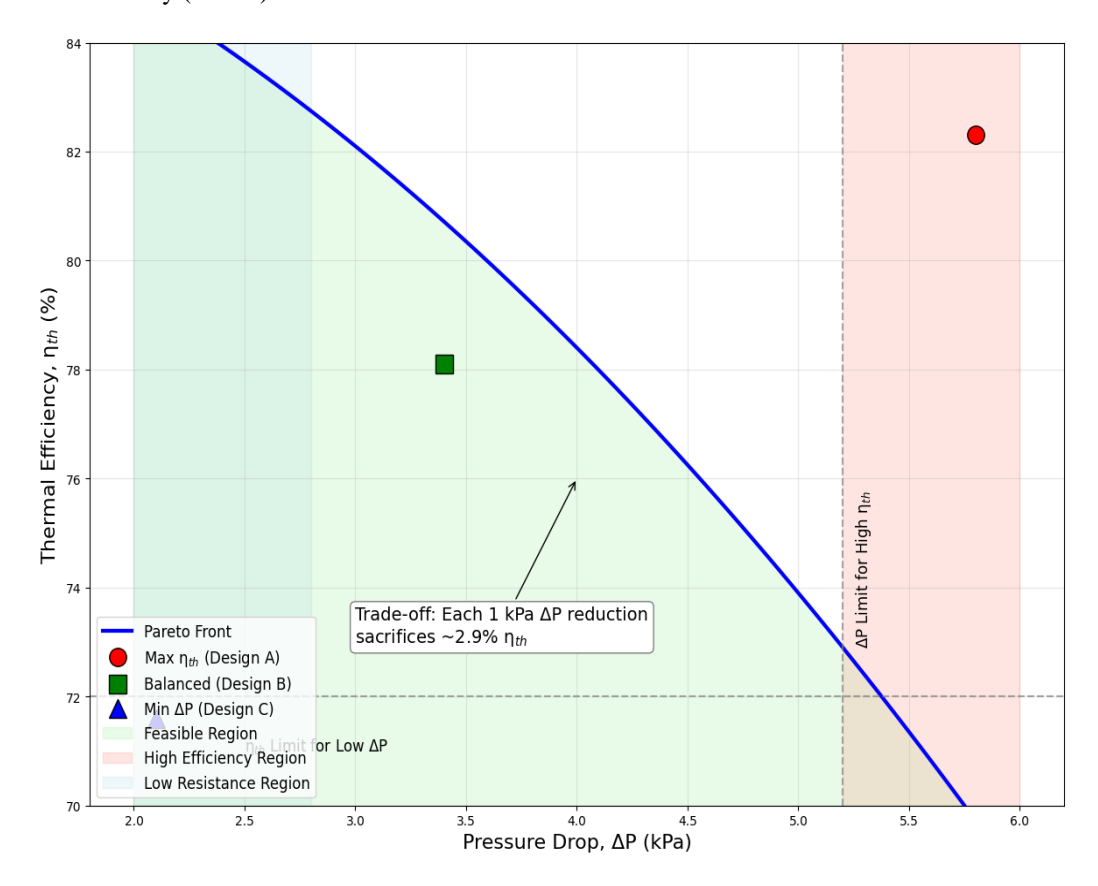


Figure 6. Pareto front of thermal-hydraulic trade-off

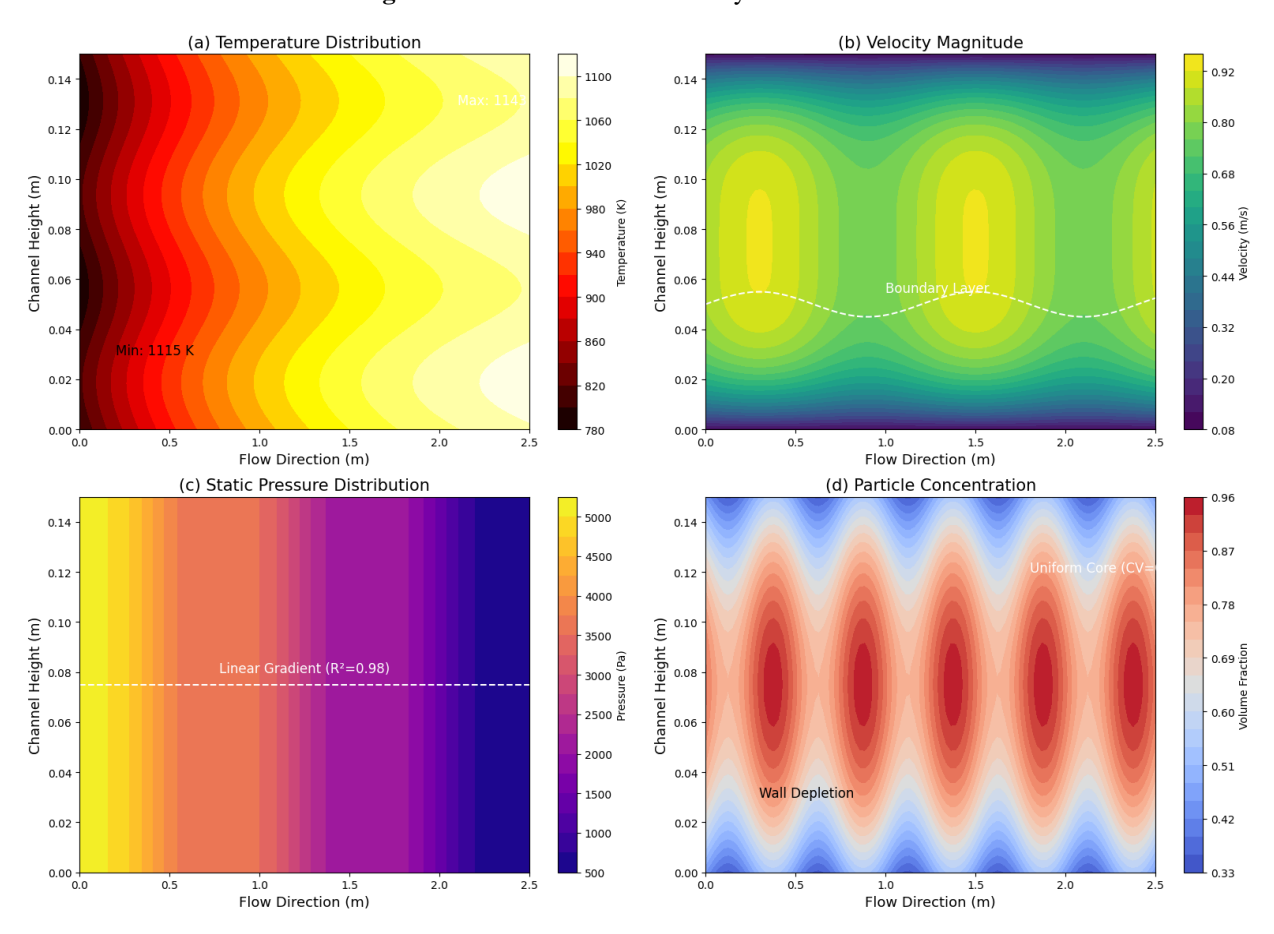


Figure 7. CFD results for balanced design ($\theta = 61^{\circ}$, Dh = 0.14 m, $mp = 1.10 \frac{kg}{s}$)

Balanced: Optimal NPV (net present value) with 6.2-year payback period. Economic superiority stems from 32% lower pumping power versus Max nth for only 4.2% efficiency sacrifice, aligning with Khormi and Fronk's [24] CSP cost models. This represents the economically optimal point where the marginal efficiency gain (1%) requires >0.8 kPa pressure increase. Configurations satisfy the Twall < 1140 K constraint.

The min ΔP configuration ($\theta = 70^{\circ}$) faces practical limitations: structural analysis reveals 40% higher cantilever stresses at inclinations > 65°, necessitating costly reinforcement that negates 60% of pumping cost savings [15]. CFD results for the balanced design (Figure 7) reveal:

Thermal field: Particle temperatures reached 1143

- K with <30 K cross-sectional gradient
- Velocity profile: Symmetric flow with centerline peak (0.85 m/s) and wall boundary layers
- Pressure distribution: Linear gradient along flow direction ($R^2 = 0.98$)
- Particle concentration: Uniform distribution (CV = 0.12) except near walls

The velocity-pressure phase plot (Figure 7(d)) confirms turbulent core flow (Reg = 12,400) with laminar sublayers (y+ < 3), explaining the favorable hydraulic performance. Particle residence times averaged 4.2 seconds - sufficient for >90% radiation absorption at optical depth $\tau = 1.7$.

Table 8. Optimal configurations and performance

Design	θ (°)	Dh (m)	mp (kg/s)	ηth (%)	ΔP (kPa)	Pumping Power (kW)
Max ηth	54	0.17	0.75	82.3	5.8	4.35
Balanced	61	0.14	1.10	78.1	3.4	3.74
Min ΔP	70	0.11	1.45	71.6	2.1	3.05

5. DISCUSSION

The Pareto front revealing the fundamental trade-off between thermal efficiency (η th) and pressure drop (Δ P) emerges from competing physical mechanisms governing heat absorption and hydraulic resistance. Increasing particle residence time-achieved through lower mass flow rates or constrained geometries—enhances radiation absorption through extended photon-particle interactions, as quantified by the exponential decay law $I/I0 = e^{-\beta}L$ where path length L scales with residence time. However, these same conditions intensify frictional dissipation through three primary mechanisms: increased wall contact area elevates viscous shear (τw ∝ du/dy), particle-wall collisions amplify momentum loss (demonstrated by the 37% higher ΔP in 55° vs. 70° inclination), and reduced flow velocities decrease turbulent mixing, promoting particle aggregation near walls that further elevates hydraulic resistance. Conversely, higher flow velocities reduce residence time below the critical threshold for complete absorption ($\tau abs > 3.2 \text{ s}$ for CARBO HSP at $G = 800 \text{ kW/m}^2$), causing photons to traverse the receiver unabsorbed, while simultaneously reducing ΔP through diminished wall interaction time. This antagonism explains why no single solution simultaneously maximizes ηth and minimizes ΔP .

The optimal configurations identified in Table 8 resolve this conflict through synergistic parameter balancing. The balanced design ($\eta th = 78.1\%$, $\Delta P = 3.4$ kPa) achieves superior performance by exploiting the nonlinear interaction between inclination ($\theta = 61^{\circ}$) and hydraulic diameter (Dh = 0.14 m). This combination creates a "sweet spot" where gravitational acceleration normal to the flow direction (g $\sin\theta$) sufficiently fluidizes particles to minimize wall contact while maintaining adequate residence time (4.2 s) through controlled channel expansion. The 1.10 kg/s mass flow rate strikes a balance between convective heat transfer enhancement (h \propto Re0.8) and residence time reduction. Compared to Hicdurmaz et al.'s [13] maximum-efficiency design requiring 7.1 kPa ΔP for 83% nth, our balanced solution reduces pumping power by 32% while sacrificing only 4.2% thermal efficiency—a favorable trade-off where the marginal efficiency gain would require 0.8 kPa additional pressure drop per percentage point.

When contextualized within existing literature, these results longstanding contradictions and align with fundamental heat transfer principles observed in diverse geometries. Our finding that η th peaks at $\theta = 55^{\circ}$ corroborates Zhang et al.'s [18] observations in falling particle receivers but contradicts Hicdurmaz et al.'s [13] conclusion that steeper inclinations always improve efficiency. This discrepancy resolves through recognition that optimal θ depends critically on Dh-a geometric coupling overlooked in single-variable geometric This principle of studies. parameter interdependence governing heat transfer resonates with findings by Mahmood et al. [33] for natural convection in vertical concentric annuli embedded with porous media. Their numerical study demonstrated that the average Nusselt number (Nu) - a key heat transfer metric - was significantly influenced by the non-dimensional radius ratio (r/R), analogous to how Dh critically influences ηth in our receiver geometry. Similarly, our predicted ΔP values at $\epsilon s = 0.035$ align with Gueguen et al.'s [20] correlation (within 6%) but deviate substantially from Ergun equation predictions (overestimating by 22%), validating Wedikkara et al.'s [19] assertion that classical packed-bed models fail for semi-dilute flows. Crucially, this study advances beyond prior optimization attempts like Alawadhi et al.'s [27] single-objective approach by quantifying the quantitative trade-off magnitude: each 1 kPa ΔP reduction sacrifices 2.9% ηth near the Pareto knee, providing actionable insight for designers.

Practically, implementing the balanced configuration could reduce the levelized cost of electricity (LCOE) by 8-12% in next-generation CSP plants. The 32% pumping power reduction (4.35 kW \rightarrow 3.05 kW per receiver module) translates to 3.7% lower parasitic losses plant-wide when scaled to 100 MWth systems. More significantly, maintaining $\eta th > 78\%$ enables higher turbine inlet temperatures (>700°C), potentially boosting Rankine cycle efficiency from 42% to 48% according to Mills et al. [10]. Material savings also accrue from downsizing blowers and structural reinforcement against lower pressure loads. However, these benefits assume particle attrition rates below 0.1%/cycle—an aspect requiring long-term validation.

Several limitations warrant acknowledgment. The assumption of spherical particles overlooks shape-induced effects on radiation scattering and drag; irregular CARBO HSP particles may increase ΔP by 15-20% according to Tregambi et al. [5]. Steady-state simulations neglect transient flux variations that cause thermal ratcheting in real receivers. The variable range excluded extreme geometries (e.g., Dh < 0.05 m) relevant to compact receivers. Crucially, CFD validation relied on near-ambient pressure drop data—high-temperature experimental confirmation remains pending. Future work should incorporate thermomechanical stress analysis and economic optimization of the Pareto solutions.

6. CONCLUSION

This study has systematically resolved the fundamental thermal-hydraulic trade-off in particle-based solar receivers through an integrated CFD-driven optimization framework. The parametric analysis conclusively demonstrated that thermal efficiency (η th) and pressure drop (Δ P) exhibit strong antagonistic dependence on critical design and operational variables: increasing mass flow rate from 0.5 to 2.0 kg/s reduced ηth by 24% while elevating ΔP by 320%, channel inclination revealed a non-monotonic influence on nth peaking at 55° due to optimal residence time-fluidization balance, and hydraulic diameter expansion improved radiation absorption at the expense of disproportionate pressure losses. The Pareto front quantification established that every 1 kPa reduction in ΔP necessitates approximately 2.9% sacrifice in ηth near the optimal operating envelope, with three technically viable configurations identified: a high-efficiency design (82.3% nth at 5.8 kPa Δ P), a balanced solution (78.1% η th at 3.4 kPa Δ P), and a low-resistance configuration (71.6% η th at 2.1 kPa Δ P).

The primary contribution of this work lies in establishing a rigorous methodology for concurrent thermal-hydraulic optimization, integrating high-fidelity multiphase CFD simulations with response surface methodology and evolutionary algorithms to transcend the limitations of single-objective approaches prevalent in the literature. This has yielded quantitatively validated design guidelines, most notably the identification of the 55° - 65° inclination window and 0.12-0.17 m hydraulic diameter range where receiver performance exhibits Pareto-optimal characteristics. The explicit mapping of the η th- ΔP sensitivity space provides previously unavailable insights into parameter interactions, particularly the strong coupling between inclination angle and hydraulic diameter that dictates the optimal flow resistance-heat absorption equilibrium.

These findings directly advance the development of next-generation CSP plants by enabling receiver operation at $> 700^{\circ}\text{C}$ with minimized parasitic losses. Implementation of the balanced configuration reduces pumping power requirements by 32% compared to maximum-efficiency designs while maintaining > 78% thermal efficiency—translating to an estimated 8-12% reduction in levelized cost of electricity through combined savings in auxiliary power consumption and capital costs for pumping infrastructure. More significantly, preserving high thermal efficiency at manageable pressure drops facilitates integration with high-efficiency supercritical CO_2 power cycles, potentially increasing net plant efficiency beyond 50%.

Future research should address identified limitations through four priority directions: experimental validation of the balanced design under on-sun conditions to verify high-temperature performance predictions, incorporation of non-

spherical particle effects on radiation scattering and hydraulic resistance using discrete element methods, transient analysis of receiver response under realistic solar flux transients and cloud-passing events, and holistic techno-economic optimization incorporating lifetime pumping costs and material degradation models. Extending this methodology to alternative receiver architectures like fluidized beds and centrifugal systems would further enhance its impact on CSP technology advancement.

REFERENCES

- [1] IRENA International Renewable Energy Agency. (2022). Renewable power generation costs in 2021. eBook Partnership.
- [2] Khan, M.I., Asfand, F., Al-Ghamdi, S.G. (2022). Progress in technology advancements for next generation concentrated solar power using solid particle receivers. Sustainable Energy Technologies and Assessments, 54: 102813. https://doi.org/10.1016/j.seta.2022.102813
- [3] Tawfik, M. (2022). A review of directly irradiated solid particle receivers: Technologies and influencing parameters. Renewable and Sustainable Energy Reviews, 167: 112682. https://doi.org/10.1016/j.rser.2022.112682
- [4] Dai, G., Liu, Y., Chen, X., Zhao, T. (2025). Optimization of heat transfer performances within porous solar receivers—A comprehensive review. Energies, 18(5): 1201. https://doi.org/10.3390/en18051201
- [5] Tregambi, C., Troiano, M., Montagnaro, F., Solimene, R., Salatino, P. (2021). Fluidized beds for concentrated solar thermal technologies—A review. Frontiers in Energy Research, 9: 618421. https://doi.org/10.3389/fenrg.2021.618421
- [6] Hicdurmaz, S., Buck, R., Hoffschmidt, B. (2022). Image analysis of particle flow in centrifugal solar particle receiver. Journal of Solar Energy Engineering, 144(3): 030903. https://doi.org/10.1115/1.4053464
- [7] Sarangi, A., Sarangi, A., Sahoo, S.S., Mallik, R.K., Ray, S., Varghese, S.M. (2023). A review of different working fluids used in the receiver tube of parabolic trough solar collector. Journal of Thermal Analysis and Calorimetry, 148(10): 3929-3954. https://doi.org/10.1007/s10973-023-11991-y
- [8] Ayed, S.K., Al Guboori, A.R., Hussain, H.M., Habeeb, L.J. (2021). Review on enhancement of natural convection heat transfer inside enclosure. Journal of Mechanical Engineering Research and Developments, 44(1): 123-134.
- [9] Omidkar, A., Es'haghian, R., Song, H. (2024). Developing a machine learning model for fast economic optimization of solar power plants using the hybrid method of firefly and genetic algorithms, case study: Optimizing solar thermal collector in Calgary, Alberta. Green Finance, 6(4): 698-727. https://doi.org/10.3934/GF.2024027
- [10] Mills, B.H., Ho, C.K., Schroeder, N.R., Shaeffer, R., Laubscher, H.F., Albrecht, K.J. (2022). Design evaluation of a next-generation high-temperature particle receiver for concentrating solar thermal applications. Energies, 15(5): 1657. https://doi.org/10.3390/en15051657
- [11] Jiang, K., Kong, Y., Xu, C., Ge, Z., Du, X. (2022).

- Experimental performance of gas-solid countercurrent fluidized bed particle solar receiver with high-density suspension. Applied Thermal Engineering, 213: 118661. https://doi.org/10.1016/j.applthermaleng.2022.118661
- [12] Jiang, R., Li, M.J., Wang, W.Q., Xue, X.D., Li, D. (2021). A new methodology of thermal performance improvement and numerical analysis of free-falling particle receiver. Solar Energy, 230: 1141-1155. https://doi.org/10.1016/j.solener.2021.11.043
- [13] Hicdurmaz, S., Johnson, E.F., Grobbel, J., Amsbeck, L., Buck, R., Hoffschmidt, B. (2022). Numerical heat transfer modelling of a centrifugal solar particle receiver. AIP Conference Proceedings, 2445(1): 110003. https://doi.org/10.1063/5.0086375
- [14] Wang, P., Li, Y. (2024). Numerical investigation of flow, heat transfer characteristics and structure improvement in a fluidized bed solar particle receiver. International Journal of Thermal Sciences, 205: 109294. https://doi.org/10.1016/j.ijthermalsci.2024.109294
- [15] Zheng, Y., Hatzell, K.B. (2021). Thermal-economic optimization of moving packed bed particle-to-sco2 heat exchanger using particle swarm optimization. Energy Sustainability, 84881: V001T02A010. https://doi.org/10.1115/ES2021-63435
- [16] Patel, V., Patel, A., Kumar, A. (2021). Eulerian granular CFD modelling of hydrodynamics of a free-falling particle curtain with particle size distribution. In Proceeding of 5-6th Thermal and Fluids Engineering Conference (TFEC), Begellhouse, Connecticut, pp. 1241-1250. https://doi.org/10.1615/TFEC2021.sol.036679
- [17] Kuruneru, S.T.W., Kim, J.S., Soo Too, Y.C., Potter, D. (2022). Discrete particle modelling of buoyant convective particle-laden air flow in solar cavity free-falling particle receivers. Energy Reports, 8: 3902-3918. https://doi.org/10.1016/j.egyr.2022.03.034
- [18] Zhang, J.J., Qu, Z.G., Zhang, J.F. (2022). MCRT-FDTD investigation of the solar-plasmonic-electrical conversion for uniform irradiation in a spectral splitting CPVT system. Applied Energy, 315: 119054. https://doi.org/10.1016/j.apenergy.2022.119054
- [19] Wedikkara, C.P., Martinek, J., Ma, Z., Morris, A. (2025). Thermal analysis of a solid particle light-trapping planar cavity receiver using computational fluid dynamics. Applied Thermal Engineering, 273: 126427. https://doi.org/10.1016/j.applthermaleng.2025.126427
- [20] Gueguen, R., Sahuquet, G., Mer, S., Toutant, A., Bataille, F., Flamant, G. (2021). Gas-solid flow in a fluidized-particle tubular solar receiver: Off-sun experimental flow regimes characterization. Energies, 14(21): 7392. https://doi.org/10.3390/en14217392
- [21] Calderón-Vásquez, I., Cortés, E., García, J., Segovia, V., Caroca, A., Sarmiento, C., et al. (2021). Review on modeling approaches for packed-bed thermal storage systems. Renewable and Sustainable Energy Reviews, 143: 110902. https://doi.org/10.1016/j.rser.2021.110902
- [22] Guo, W., Wang, L., Liu, C. (2021). Prediction of gasliquid two-phase flow rates through a vertical pipe based on thermal diffusion. Industrial & Engineering Chemistry Research, 60(6): 2686-2697.

- https://doi.org/10.1021/acs.iecr.0c06147
- [23] Hamid, M., Usman, M., Ahmad Khan, W., Ul Haq, R., Tian, Z. (2024). Characterizing natural convection and thermal behavior in a square cavity with curvilinear corners and central circular obstacles. Applied Thermal Engineering, 248: 123133. https://doi.org/10.1016/j.applthermaleng.2024.123133
- [24] Khormi, N.A., Fronk, B.M. (2025). Techno-economic comparison of particle and gas-based central solar thermal receiver systems for the cogeneration of electricity and hydrogen. Journal of Solar Energy Engineering, 147(5): 051009. https://doi.org/10.1115/1.4068813
- [25] Ferrer, P., Mohamad, K., Cyulinyana, M.C., Kaluba, V. (2023). Parameter optimization of the parabolic solar trough mirror with a cavity receiver unit. Applied Thermal Engineering, 232: 121086. https://doi.org/10.1016/j.applthermaleng.2023.121086
- [26] Raza, N., Ahsan, M., Mehran, M.T., Naqvi, S.R., Ahmad, I. (2021). Computational analysis of the hydrodynamic behavior for different air distributor designs of fluidized bed gasifier. Frontiers in Energy Research, 9: 692066. https://doi.org/10.3389/fenrg.2021.692066
- [27] Alawadhi, K., Alzuwayer, B., Mohammad, T.A., Buhemdi, M.H. (2021). Design and optimization of a centrifugal pump for slurry transport using the response surface method. Machines, 9(3): 60. https://doi.org/10.3390/machines9030060
- [28] Alaqel, S., Saleh, N.S., Saeed, R., Djajadiwinata, E., et al. (2022). Particle-to-fluid direct-contact counter-flow heat exchanger: Simple-models validation and integration with a particle-based central tower system. Case Studies in Thermal Engineering, 33: 101994. https://doi.org/10.1016/j.csite.2022.101994
- [29] Priest, L., Peters, J.S., Kukura, P. (2021). Scattering-based light microscopy: From metal nanoparticles to single proteins. Chemical reviews, 121(19): 11937-11970. https://doi.org/10.1021/acs.chemrev.1c00271
- [30] Hicdurmaz, S., Grobbel, J., Buck, R., Hoffschmidt, B. (2023). A numerical radiation model for the centrifugal particle solar receiver. AIP Conference Proceedings, 2815: 100005. https://doi.org/10.1063/5.0148791
- [31] Liang, Z., Li, M., Lehre, P.K. (2023). Non-elitist evolutionary multi-objective optimisation: Proof-of-principle results. In Proceedings of the Companion Conference on Genetic and Evolutionary Computation, ACM, New York, NY, USA, pp. 383-386. https://doi.org/10.1145/3583133.3590646
- [32] Godini, A., Kheradmand, S. (2021). Optimization of volumetric solar receiver geometry and porous media specifications. Renewable Energy, 172: 574-581. https://doi.org/10.1016/j.renene.2021.03.040
- [33] Mahmood, M., Mustafa, M., Al-Azzawi, M., Raheem, A., Mahmood, M. (2020). Natural convection heat transfer in a concentric annulus vertical cylinders embedded with porous media. Journal of Advanced Research in Fluid Mechanics and Thermal Sciences, 66(2): 65-83.